Chapter 2

Methods

This chapter outlines the synthesis procedure and experimental techniques employed in this thesis. Sample preparation was carried out using the standard arc melting furnace. Structural studies were carried out using both conventional X-ray diffraction and synchrotron X-ray powder diffraction techniques. Magnetization and magnetotransport measurements were conducted with a physical properties measurement system (PPMS). The principles and procedures of these experimental techniques are discussed in detail in this chapter.

2.1 Synthesis

The samples were prepared using the conventional arc melting technique, commonly used to melt metals and produce alloys in an inert atmosphere. This process was followed by annealing under vacuum condition. The complete sample preparation setup is shown in Fig. 2.1(a). This method involves heating via an electric arc formed between a tungsten electrode and the metal piece placed in a copper crucible. The electric arc is produced through the application of high voltage to the tungsten tip, reaching temperatures up to 3000 °C, which is sufficient to melt most metals to form metallic samples. The arc-melting setup consists of three main components: an arc melting furnace equipped with a rotary pump, a power source, and a chiller. A magnefied view of the arc melting furnace is shown in Fig. 2.1(b). The rotary pump is used to evacuate the chamber of the arc melting furnace to a pressure as low as 10^{-3} mbar before melting. The power source is used to apply high electric voltage to the tungsten tip. The chiller is used to protect both the copper hearth and the tungsten tip from melting during the high-temperature process. High-purity (99.99 %) pieces of raw elements are placed inside the crucibles on the copper hearth. Before melting the raw elements, a titanium (Ti) getter ball (∼5 g) is first melted to absorb trace oxygen molecules in the chamber, forming a TiO_2 layer on its surface. Once this process is complete, the elements in the crucible are melted to form the alloy. The alloy is then melted repeatedly, typically 4 to 6 times, flipping it to confirm homogeneous mixing. After melting, the weight of the sample is measured, with a weight loss of less than 1% observed for all the studied systems. The samples are annealed in a box furnace capable of

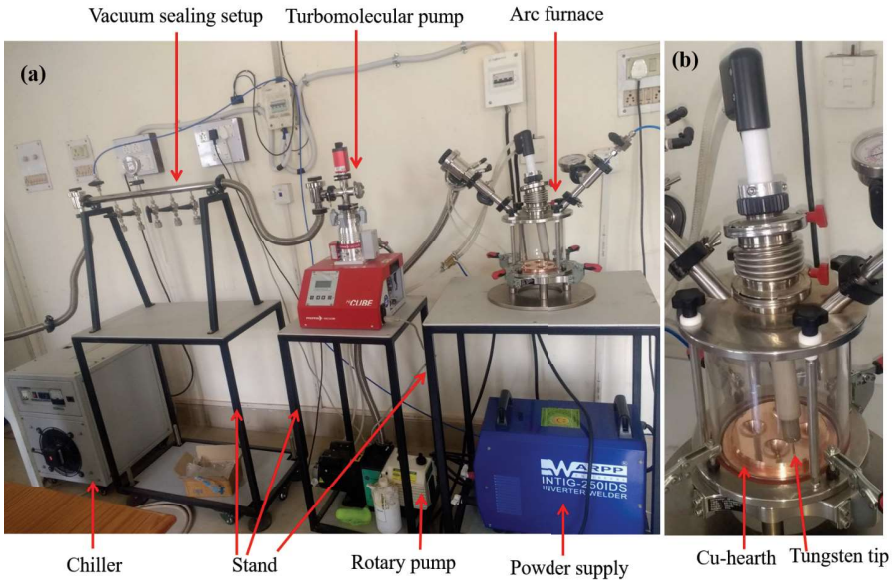

Figure 2.1: (a) A real image of sample preparation setup. (b) A zoomed view of the arc melting furnace.

reaching temperatures up to 1400 °C. The annealing process begins with sealing the sample inside a quartz tube in an inert gas (argon) atmosphere, which is previously pumped to a vacuum level of 10^{-6} mbar with a diffusion/turbomolecular pump. The sealed ampule is then placed in the furnace for annealing at the specified temperature and duration, followed by quenching in ice water.

2.2 X-ray diffraction

X-ray diffraction (XRD) is a highly effective analytical tool for studying the crystal structure of materials. When X-rays strike the surface of a crystal, they interact with the atomic structure and diffract in various directions. X-rays are electromagnetic radiation with much shorter wavelengths than visible light. They were discovered by Wilhelm Conrad Röntgen in 1895, and their ability to penetrate various materials made them particularly valuable in scientific and medical fields. The wavelength of X-rays typically ranges from 0.1 Å to 100 Å. These shorter wavelengths (similar to the distance between atoms in a unit cell) allow X-rays to interact with the atomic structure of materials, which is the basis for techniques [1]. In 1912, Max von Laue proposed the principle behind XRD. He suggested that if atoms in a crystal were arranged in a regular, periodic pattern, they could interact

with X-rays in a way similar to how light interacts with a diffraction grating [2, 3]. In

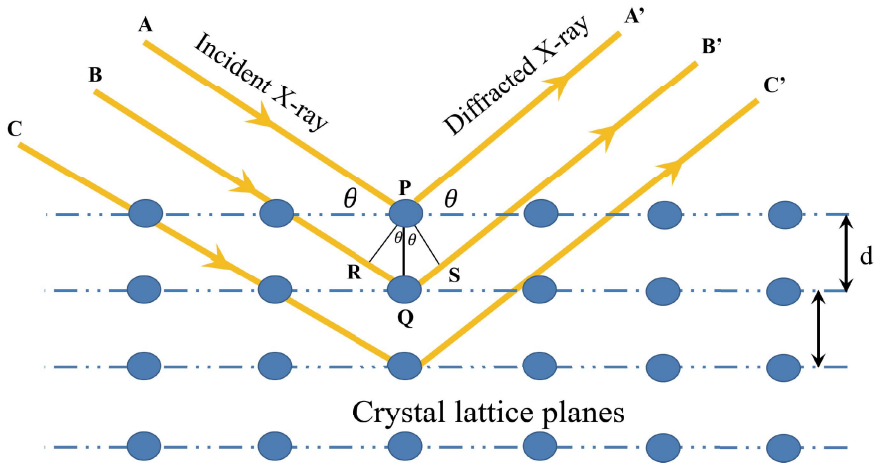

Figure 2.2: X-ray diffraction by the crystal planes of a crystal

1914, Max von Laue discovered the diffraction of X-rays by crystals. He demonstrated that when X-rays pass through a crystalline material, they are scattered in specific patterns due to the regular arrangement of atoms in the crystal [2]. Following von Laue's discovery, the analysis of XRD patterns was significantly advanced by William Lawrence Bragg and William Henry Bragg. They formulated Bragg's law, which provides a mathematical relationship that describes how X-rays are diffracted by the atomic structure in a crystal. Bragg's law is expressed as[4]:

$$2dSin\theta = n\lambda \tag{2.1}$$

Here n is an integer representing the order of diffraction, (λ) is the wavelength of the incident X-ray, θ is the angle of diffraction, and d is the distance between planes in the crystal. Figure 2.2 shows the schematic diagram of incident and diffracted X-ray beam from the crystal planes based on Bragg's law. The incident beams are lebeled as A, B, and C, and the diffracted beams are lebeled as A', B', and C'. The incident beams interact with the atoms in crystal planes after satisfying the Bragg condition, and the diffracted beams are produced. These diffracted X-rays are collected by detectors. By measuring the angles and intensities of these scattered rays, a diffraction pattern is produced. The analysis of the diffraction pattern provides information of crystal structure, phase fractions, unit cell dimensions, crystallite size, microstrain, and more. In this thesis, XRD data were

collected using a laboratory X-ray machine equipped with an 18 kW rotating anode and a curved graphite crystal monochromator. A real image of the XRD machine is shown in Fig. 2.3(a), and a zoomed view of the diffractometer is presented in Fig. 2.3(b), which operates in the Bragg-Brentano geometry.

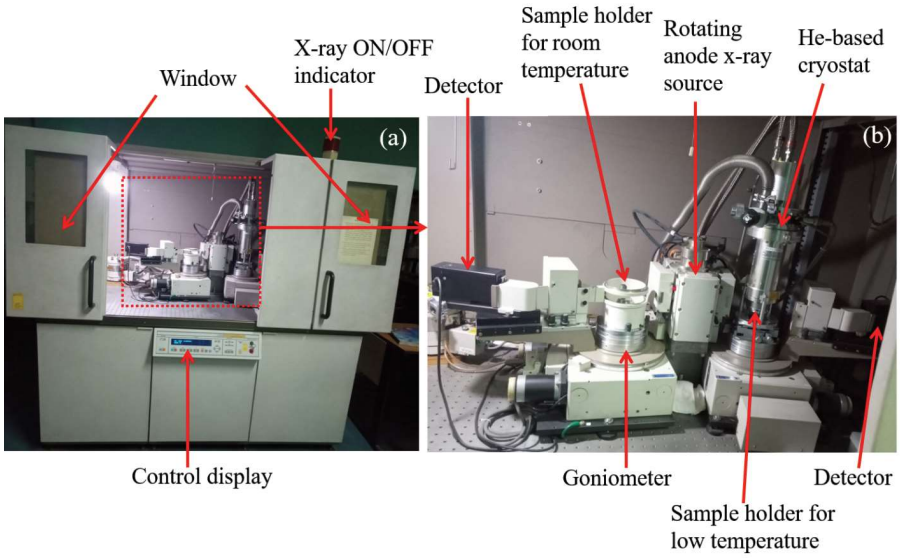

Figure 2.3: (a) A real image of Rigaku X-ray diffractometer (at the School of Materials Science and Technology). (b) A zoomed view of the diffractometer.

2.3 Synchrotron X-ray diffraction measurements

Synchrotron radiation is a type of electromagnetic radiation produced when high-energy electrons are accelerated, specifically when they are forced to travel along a curved path (usually in a circular or spiral orbit) under the influence of magnetic field [5, 6]. It operates on the principle that an accelerated charge emits radiation; for example, when a moving electron changes direction, it releases electromagnetic radiation [7, 8]. The use of synchrotron-based X-ray sources offers numerous advantages over conventional X-ray sources, including high energy, increased brilliance, a broader energy spectrum, wavelength adjustability, strong polarization, and ultra-short pulse emissions [5, 9]. Consequently, synchrotron X-ray diffraction (SXRD) measurement enables the characterization of material's structures with significantly greater detail compared to conventional XRD [7, 8, 10]. There are different components involved in the generation of synchrotron-

based X-rays, as depicted by a schematic diagram in Fig. 2.4. These components are linear accelerator, booster ring, storage ring, and beamlines.

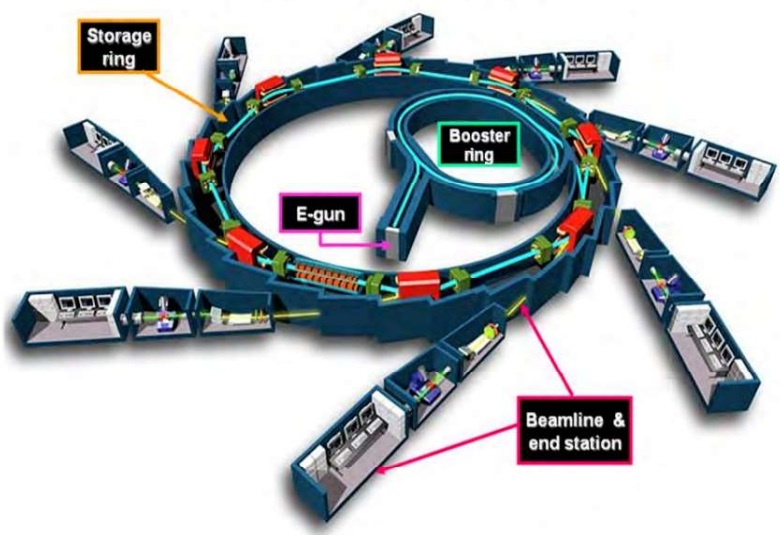

Figure 2.4: A schematic diagram of the synchrotron X-ray source and beamline [11].

2.3.1 Linear accelerator

A linear accelerator in a beamline is used to accelerate charged particles, such as electrons, to high energies (MeV) along a straight path. It employs a series of oscillating electric field to increase the particle energy in stages while maintaining a precise trajectory. The accelerated beam is then directed towards experimental targets or further systems for applications like materials research. Linacs are known for their compact design and ability to produce highly focused and energetic beams [8, 12].

2.3.2 Booster ring

The booster ring in a beamline is an intermediate accelerator that increases the energy of the electrons before injecting them into the storage ring. Electrons are first introduced into the booster ring at relatively low energies and then accelerated to higher energies (GeV). This process ensures a stable and high-energy electron beam suitable for synchrotron radiation production. The booster ring operates in a cyclic manner, periodically filling the storage ring with new energetic electrons. It plays a critical role in maintaining the effi-

ciency and performance of the overall beamline system [8, 12].

2.3.3 Storage ring

The storage ring in a beamline is a circular accelerator where high-energy electrons are stored and maintained for extended periods under ultra-high vacuum condition. As the electrons circulate, they are steered and focused by bending magnets and undulators, which cause them to emit synchrotron radiation. This radiation, spanning wavelengths from infrared to X-rays, is extracted through beamlines for various scientific applications. The storage ring's design ensures stable, intense, and continuous radiation, enabling precise and high-quality experimental results. It serves as the core component of a synchrotron radiation source, supporting advanced research in fields like materials science, biology, and physics [8, 12].

2.3.4 Beamlines

Beamlines are specialized pathways that transport synchrotron radiation from the storage ring to experimental stations. The emitted X-rays are directed to the experimental hutch through beamlines, which are equipped with mirrors, monochromators, slits, and focusing devices. These components ensure that the X-ray beam is precisely tailored and focused on the sample for accurate material characterization [8, 12].

2.4 P02.1 beamline of PETRA-III

Figure 2.5(a) illustrates a schematic of the P02.1 beamline at PETRA-III, DESY, Germany, showing the X-ray path from the undulator to the detector via the sample. Using this technique, temperature-dependent powder XRD patterns were recorded. It operates using high-energy X-rays (60 keV, wavelength $\lambda \sim 0.2071$ Å) [11, 13]. For synchrotron X-ray powder diffraction (SXRPD) measurements, borosilicate capillaries were used as sample containers, with fine powder samples packed into the capillaries and spun continuously during measurements to reduce texturing effects in the data. Figure 2.5(b) shows

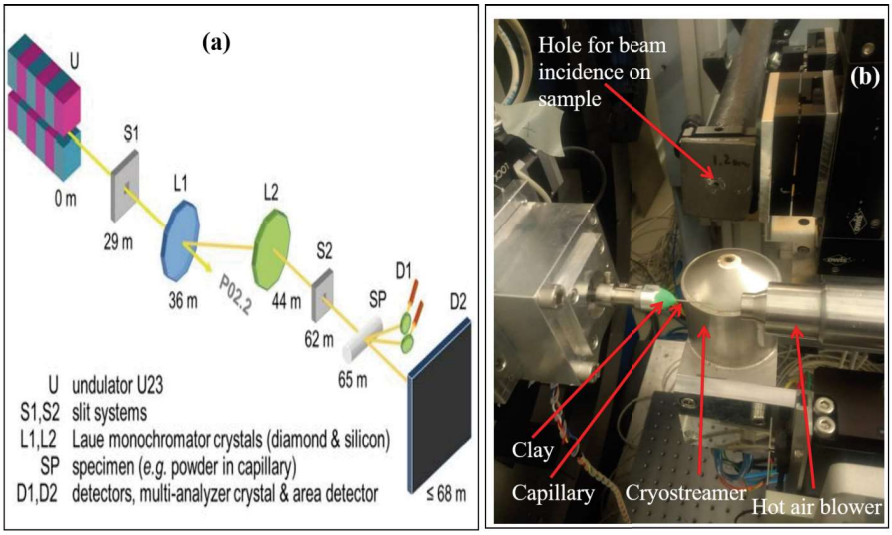

Figure 2.5: (a) An illustration of optics of the beamlines at PETRA-III. [11]. (b) A real image of the P02.1 beamline station.

a mounted capillary ready for diffraction measurements at the P02.1 beamline. Data was collected in transmission mode based on the Debye-Scherrer geometry using a 2D detector (Perkin Elmer, pixel size (200 X 200 μm^2). High-resolution SXRPD data were acquired by positioning the 2D detector at distance ∼1200–1500 mm from the sample , while high-Q pair distribution function (PDF) data were obtained by moving the detector closer to the sample (i.e. sample to detector distance ∼200–400 mm) to capture higher-angle Debye cones. Background contributions were removed by collecting high-Q data for empty borosilicate capillaries. Temperature variation (100–400 K) was achieved using a nitrogen cryostream directed to the capillary. The raw 2D diffraction images were integrated into 1D diffraction patterns (intensity vs. 2θ) using the Fit2D [14] and Dawn-Diamond software programs [15].

2.5 Xpress beamline of Elettra

Pressure-dependent powder XRD patterns were recorded at the Xpress beamline using high-energy X-rays (25 keV, $\lambda \sim 0.495$ Å). High resolution SXRPD data was collected up to 14 GPa using a membrane-driven diamond anvil cell (DAC). Figure 2.6(a) presents the synchrotron radiation source and beamlines at Elettra and (b) illustrates a schematic of the DAC, highlighting the positions of its components. In this experiment, a mixture

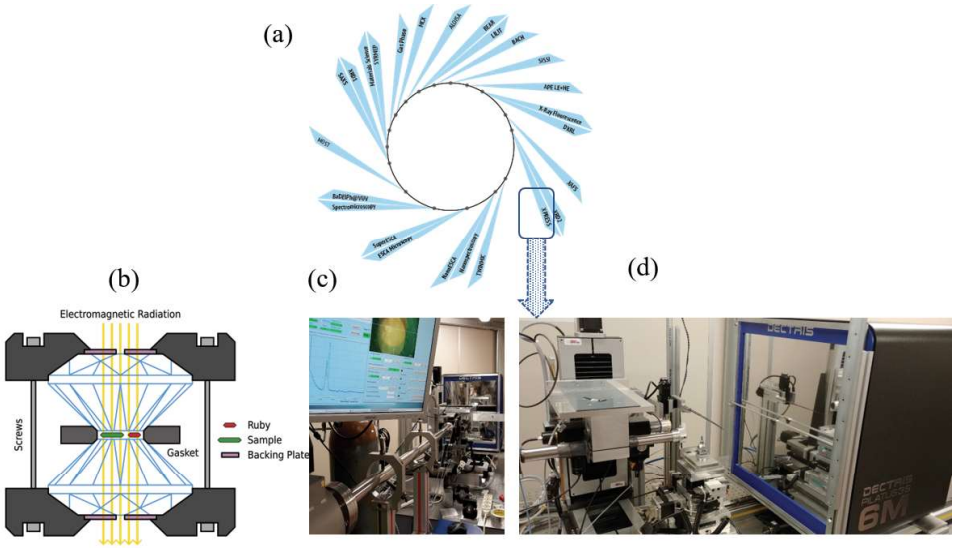

Figure 2.6: (a) A schematic diagram of the synchrotron radiation source and beamlines at Elettra. (b) Schematic diagram of diamond anvil cell (DAC). Figs. (c,d) show the real image of the experimental hutch and detector at the Xpress beamline.

of methanol and ethanol in a 4:1 ratio was used to transmit the pressure inside a DAC. The DAC is designed to create extremely high pressures by squeezing a small sample between two diamonds. To measure the pressure inside the DAC, the ruby fluorescence method was employed. This technique relies on the properties of tiny ruby chips. These chips are small crystals, $\sim$ 5-10 μm in size. The ruby chips are placed alongside the sample inside the pressure chamber of the DAC. When the pressure changes, the fluorescence (the emission of light) from the ruby chips also changes in a measurable way. This allows to accurately monitor the pressure within the chamber by observing the fluorescence emitted from the ruby chips under specific conditions. Figs. 2.6(c,d) show the experimental hutch and detector at the Xpress beamline, respectively.

2.6 Magnetization measurements

Magnetization measurements were carried out to investigate the magnetic properties of the samples as a function of the applied magnetic field [$M(H)$] and the temperature [$M(T)$]. These measurements were conducted using the PPMS, a versatile experimental setup designed for precise characterization of various physical properties under controlled conditions. They provide insights into saturation magnetization, phase transition temperatures,

and the magnetocaloric effect. This system is equipped with a vibrating sample magnetometer (VSM) linear motor transport head to vibrate the sample, a gradiometer pickup coil to detect flux changes, various electronic components to control the motor and process the coil's response, and MultiVu software for automated operation [16–18]. In the VSM, the magnetic sample vibrates within a uniform magnetic field generated by a superconducting magnet near the detection coil. A non-magnetic rod supports the sample at one end, while a linear motor is affixed to the other. The vibration causes a change in magnetic flux in the detection coil, inducing a voltage according to Faraday's law of induction. The magnitude of this voltage is directly proportional to the magnetic moment of the sample. The induced voltage is then amplified and precisely measured using a lock-in amplifier. The VSM has a sensitivity of $<10^{-6}$ emu, i.e., it is able to resolve magnetization changes of less than $<10^{-6}$. Generally, the vibration frequency remains below 40 Hz, with a vibration amplitude that typically measures a few millimeters.

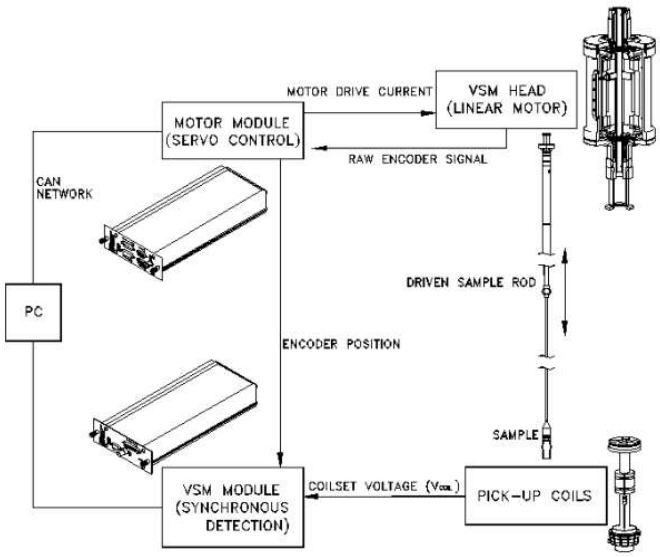

Figure 2.7: Operation of the vibrating sample magnetometer (VSM) within a superconducting solenoid [17].

2.6.1 Theory of operation

In a superconducting quantum interference device (SQUID) VSM, the flux change generated by the vibration of the sample near the coil is directly transmitted to the SQUID

via a gradiometer coil, where it is converted into a voltage. This voltage is plotted as a flux profile based on the position of the sample. The magnetization is then calculated by fitting this profile to the expected behavior of a point dipole.

According to Faraday's law, a time-dependent change in magnetic flux generates an induced voltage in the coil. The induced voltage as a function of time is described by:

$$V_{coil} = \left(\frac{d\phi}{dt}\right) = \left(\frac{d\phi}{dz}\right)\left(\frac{dz}{dt}\right) \tag{2.2}$$

here, dϕ represents the magnetic flux through the pickup coil, z denotes the vertical position of the sample relative to the coil, and t corresponds to the time associated with the varying magnetic field. If the sample oscillates sinusoidally with respect to the coil, the induced voltage can be represented by the following equation:

$$V_{coil} = 2\pi f C_c A' m sin(2\pi f t) \tag{2.3}$$

here, C_c represents the coupling constant, m is the DC magnetic moment of the sample, A' denotes the oscillation amplitude, and f is the oscillation frequency. To determine the magnetic moment, the measurement involves fitting the sinusoidal voltage coefficients from the coil. A diagram of the VSM setup for magnetization measurement is presented in Fig. 2.7

2.7 Transport measurements

Transport measurements such as resistivity, magnetoresistance, and Hall effect, were conducted using the electrical transport option in the PPMS (Quantum Design). This system offers a versatile platform for performing various transport measurements across different resistance ranges and sample types. It features two independent channels, each equipped with dedicated electronics, enabling simultaneous and continuous resistance measurements of two separate samples. Each channel includes a precision current source and voltage preamplifiers connected to a digital signal processor (DSP) [19]. Measurements are

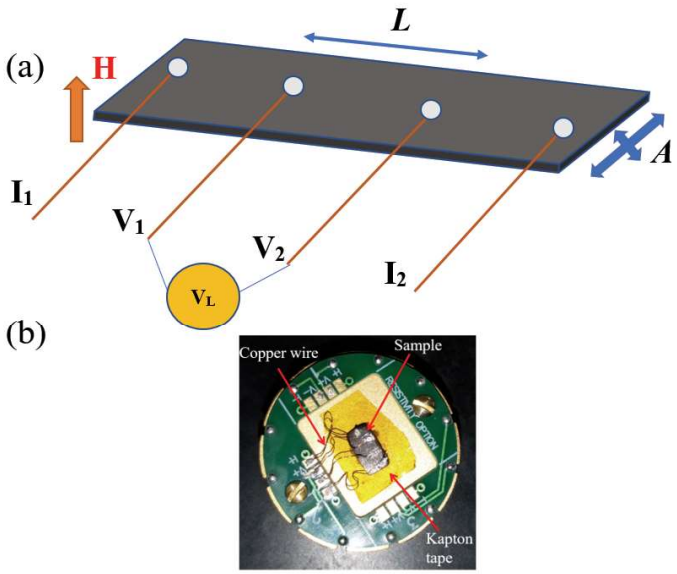

Figure 2.8: (a) A typical schematic diagram of four probe connections for longitudinal resistivity measurement. (b) A real image of a sample mounted on puck for the longitudinal resistivity measurement.

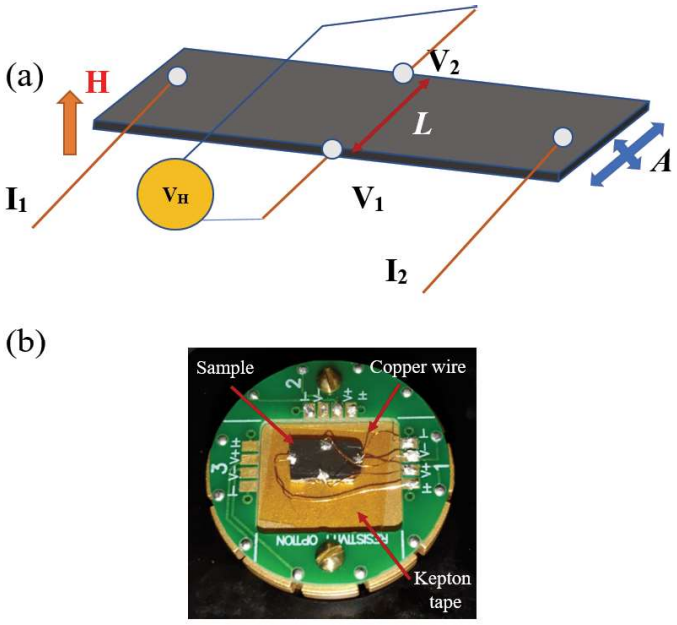

Figure 2.9: (a) A typical schematic diagram of four probe connections for transverse resistivity measurement. (b) A real image of a sample mounted on puck for the transverse resistivity measurement.

typically conducted by applying AC current and recording the resulting AC voltage. The current source used in the system is highly precise, with a minimum current resolution of 1 nA, ensuring accurate control over small current variations. It also provides a maximum output of 100 mA, making it versatile enough to support a wide range of measurements,

from very low to relatively high currents. The current source is capable of delivering both direct current (DC) and alternating current (AC) across a frequency range from 0.1 Hz to 200 Hz, enabling measurements under various experimental conditions. The voltage signal generated by the sample is processed by a set of preamplifiers, which enhance the signal for further analysis. These preamplifiers include a high-gain amplifier that boosts weak signals, a programmable gain amplifier that allows for flexible adjustment of the gain depending on the measurement requirements, and a high-impedance current amplifier that ensures minimal loading of the sample while accurately measuring the current. Together, these components work to ensure that measurements are precise and reliable, providing accurate data for transport analysis across different sample types and experimental setups. For longitudinal resistivity measurements, the four-probe method was employed, with current and voltage contacts arranged in a linear configuration, as shown in Fig. 2.8(a). I_1 and I_2 represent the current, and the voltage drop is measured between V_1 and V_2, while H indicates the applied magnetic field. The rectangular-shaped thin sample used for the resistivity measurement is shown in Fig. 2.8(b). For transverse resistivity measurements, the voltage contacts were made perpendicular to the applied current, as depicted in Fig. 2.9(a). A real image of the sample mounted on puck for Hall resistivity measurements is shown in Fig. 2.9(b). The sample is fixed in the sample holder using GE varnish on kepton tape. The contact in the sample was made by soldering the copper wires using indium as a fixer because it has a low melting point (156°C). Figure 2.8(a) provides a schematic diagram of the four-probe technique, where L denotes the distance between the two inner voltage probes, and A represents the cross-sectional area of the sample. The resistivity of a rectangular sample is mathematically expressed as [20]:

$$\rho = \frac{RA}{L} \tag{2.4}$$

here, $R = V_L/I$, V_L is the voltage drop between two inner probes, and I denotes the current through the sample.

2.8 Muon spin relaxation

Muon spin relaxation (μSR) experimental technique is a local probe method to study the magnetic properties and validates the magnetic signature of the material and uses the positive muon as a probe (microscopic magnetometer) [21, 22]. This method does not provide spatial information because of the absence of quadrupole electric moment. It does not couple with the electric field, but it carries positive energy [22]. A muon is a charged particle with spin-1/2 and a mass approximately 200 times higher than that of an electron (or about nine times lighter than a proton) [21, 23, 24]. It can be considered a heavier counterpart to the electron. With a magnetic moment ∼3.18 times larger than that of a proton, muons serve as highly sensitive microscopic probes of magnetism when implanted into a material [21]. Positive muons (μ^+) are primarily used in condensed matter physics, such as magnetism and superconductivity studies, because they avoid the positively charged atomic nuclei of the host material [21].

The μSR technique is extremely sensitive to small internal magnetic fields (∼0.1 G). It is particularly effective in systems with very small ordered magnetic moments. The μSR technique is capable of measuring magnetic fluctuation rates ranging from 10^{-4} to 10^{-12} s, depending on the strength of the magnetic field at the muon site (Fig. 2.10). This unique time window fills the gap between the fluctuation rates detectable by nuclear magnetic resonance (NMR) and neutron scattering techniques [25, 26]. When employing μSR to study materials, three experimental configurations—transverse, longitudinal, and zero-

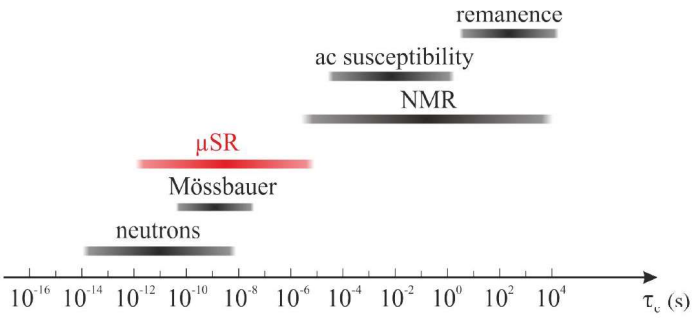

Figure 2.10: Sensitivity range of different experimental techniques [23].

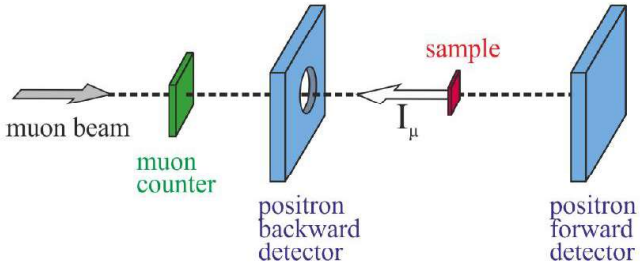

Figure 2.11: Schematic diagram of zero field configuration in μSR measurement [27].

field (ZF)—can be selected according to the orientation of the applied magnetic field. In the transverse configuration, the external magnetic field is applied in such a way that it is perpendicular to the initial direction of the muon spin polarization [23]. This configuration is useful for probing the dynamics of the magnetic environment by observing how the muon spins precess in the magnetic field. The perpendicular alignment allows for the study of transverse relaxation and fluctuation effects in the material [28]. In contrast, the longitudinal configuration involves applying the external magnetic field parallel or antiparallel to the initial muon spin polarization [23, 29]. In this configuration, the muons' spin orientation either aligns or opposes the direction of the applied field, and the behavior of the muons is directly influenced by the alignment of the magnetic field. This configuration is typically used to investigate the longitudinal relaxation processes and the effect of the magnetic field on the muon spin relaxation in materials, providing insight into the magnetic ordering and response to external field [28, 30]. In the absence of an external magnetic field, the experimental configuration is referred as zero-field muon spin relaxation (ZF-μSR) [31]. In ZF-μSR, muons are implanted into a material, and their spin behavior is monitored without the influence of any applied magnetic field. ZF-μSR is highly sensitive to subtle magnetic features within a material, making it ideal for detecting weak or localized magnetism [31]. This includes magnetism that may originate from ordered magnetic moments, where the spins of atoms align in a regular pattern, or from static and fluctuating random field that arise due to disordered magnetic interactions or impurities [31]. The sensitivity of ZF-μSR allows it to probe these weak and complex magnetic structures, which might otherwise be difficult to detect using other techniques,

such as NMR and electron paramagnetic resonance (EPR) [32]. A schematic of the ZF configuration is shown in Fig. 2.11. In the ZF configuration, the emitted positrons are counted both in the direction parallel and antiparallel to the initial spin direction of the muons [32]. The experimental setup measures the number of positrons detected in two opposite directions, typically labeled as the forward direction [F(t)] and the backward direction [B(t)]. These measurements are taken over time (t) to track how the positron emission evolves as the muon spin polarization changes. The muon spin polarization is related to the rate of change in the positron counts, providing insights into the spin dynamics of the muons and the material's internal magnetic environment. This difference is used to calculate the asymmetry of the positron emission, which is directly related to the polarization of the muons. By measuring the positron asymmetry as a function of time, it can determine how the muon spin polarization [G(t)], evolves over time in response to the local magnetic interactions. G(t) represents the relaxation of the muon polarization and provides critical information on the magnetic behavior of the material being studied, such as the presence of static or fluctuating magnetic field. G(t) is represented as follows [33]:

$$G(t) = \frac{B(t) - \alpha F(t)}{B(t) + \alpha F(t)} \tag{2.5}$$

where α is a calibration constant obtained by applying a small transverse magnetic field.

References

[1] E. Watson, "The discovery of x-rays," *Am. J. Phys.*, vol. 13, no. 5, pp. 281–291, 1945.

[2] T. Datta, "Laue: right or wrong?," *Phys. Scr.*, vol. 90, no. 3, p. 038002, 2015.

[3] B. D. Cullity, *Elements of X-ray Diffraction*. Addison-Wesley Publishing, 1956.

[4] D. C. Phillips, "William lawrence bragg, 31 march 1890-1 july 1971," 1979.

[5] S. Ebashi, M. Koch, and E. Rubenstein, "Handbook on synchrotron radiation," 1991.

[6] D. H. Bilderback, P. Elleaume, and E. Weckert, "Review of third and next generation synchrotron light sources," *J. Phys. B: At. Mol. Opt. Phys.*, vol. 38, no. 9, p. S773, 2005.

[7] A. Hofmann, *The physics of synchrotron radiation*, vol. 20. Cambridge university press, 2004.

[8] P. Willmott, *An introduction to synchrotron radiation: techniques and applications*. John Wiley & Sons, 2019.

[9] I. Munro and G. Marr, "Synchrotron radiation sources," *Handbook on Synchrotron Radiation*, vol. 2, 2013.

[10] A. Balerna and S. Mobilio, "Introduction to synchrotron radiation," in *Synchrotron Radiation: Basics, Methods and Applications*, pp. 3–28, Springer, 2014.

[11] S. K. Ali, U. Das, Y. Lu, V. Kundapur, and T. May, "Synchrotron radiation: Applications in diagnosis and treatment of malignant brain tumors," in *Diagnostic techniques and surgical management of brain tumors*, IntechOpen, 2011.

[12] A. A. Sokolov and I. M. Ternov, "Synchrotron radiation," *Akademia Nauk SSSR*, 1966.

[13] A.-C. Dippel, H.-P. Liermann, J. T. Delitz, P. Walter, H. Schulte-Schrepping, O. H. Seeck, and H. Franz, "Beamline P02.1 at PETRA III for high-resolution and high-

energy powder diffraction," *J. Synchrotron Radiat.*, vol. 22, no. 3, pp. 675–687, 2015.

[14] A. Hammersley, "Fit2d: a multi-purpose data reduction, analysis and visualization program," *J. Appl. Crystallogr.*, vol. 49, no. 2, pp. 646–652, 2016.

[15] R. Walton, A. Ashton, M. Basham, P. Chang, T. Cobb, S. da Graca, A. Dent, J. Filik, M. Gerring, C. Mita, *et al.*, "Mapping developments at diamond," *Proc. ICALEPCS*, 2015.

[16] B. D. Cullity and C. D. Graham, *Introduction to magnetic materials*. John Wiley & Sons, 2011.

[17] I. Q. Design, "Vibrating Sample Magnetometer (VSM) Option Userâ azs manual," *California, United States: Author*, 2011.

[18] S. Foner, "Vibrating sample magnetometer," *Rev. Sci. Instrum.*, vol. 27, no. 7, pp. 548–548, 1956.

[19] Q. Design, "PPMS ETO user's manual," vol. A1, pp. 1084–700, 2011.

[20] H. P. Hall, "A history of impedance measurements," *historical archives of the General Radio Company*, 1992.

[21] S. Blundell, "Spin-polarized muons in condensed matter physics," *Contemp. Phys.*, vol. 40, no. 3, pp. 175–192, 1999.

[22] J. Brewer, "Advances in muon spin rotation," 1978.

[23] A. Le Yaouanc and P. D. De Reotier, *Muon spin rotation, relaxation, and resonance: applications to condensed matter*. No. 147, OUP Oxford, 2011.

[24] G. Luke, A. Keren, L. Le, W. Wu, Y. Uemura, D. Bonn, L. Taillefer, and J. Garrett, "Muon spin relaxation in upt 3," *Phys. Rev. Lett.*, vol. 71, no. 9, p. 1466, 1993.

[25] R. H. Heffner and D. G. Fleming, "Muon spin relaxation," *Phys. Today*, vol. 37, no. 12, pp. 38–46, 1984.

[26] R. H. Heffner and K. Nagamine, "Special issue on μSR: muon spin rotation, relaxation or resonance," 2004.

[27] A. Amato, "Physics with muons: from atomic physics to solid state physics," *Lecture PHY*, vol. 432, pp. 11–17, 2018.

[28] K. JAKSETIC, "Muon spin relaxation in superconductors,"

[29] S. Blundell and S. Cox, "Longitudinal muon spin relaxation in metals and semimetals and the korringa law," *J. Phys. Condens. Matter.*, vol. 13, no. 10, p. 2163, 2001.

[30] A. D. Hillier, S. J. Blundell, I. McKenzie, I. Umegaki, L. Shu, J. A. Wright, T. Prokscha, F. Bert, K. Shimomura, A. Berlie, *et al.*, "Muon spin spectroscopy," *Nat. Rev. Methods Primers.*, vol. 2, no. 1, p. 4, 2022.

[31] R. Heffner, L. Le, M. Hundley, J. Neumeier, G. Luke, K. Kojima, B. Nachumi, Y. Uemura, D. Maclaughlin, and S.-W. Cheong, "Zero-field μ+ sr study of the colossal magnetoresistance material la 0.67 ca 0.33 mno 3," *Hyperfine Interact.*, vol. 104, pp. 29–35, 1997.

[32] P. D. De Réotier and A. Yaouanc, "Muon spin rotation and relaxation in magnetic materials," *J. Condens. Matter Phys.*, vol. 9, no. 43, p. 9113, 1997.

[33] M. Hiroi, T. Hisamatsu, T. Suzuki, K. Ohishi, Y. Ishii, and I. Watanabe, "Muon spin relaxation study of spin-glass freezing in the Heusler compound $Ru_{1.9}Fe_{0.1}CrSi$," *Phys. Rev. B*, vol. 88, no. 2, p. 024409, 2013.